Geological Magazine

www.cambridge.org/geo

Tracing wedge-internal deformation by means of strontium isotope systematics of vein carbonates

Armin Dielforder[1,2], Igor M. Villa[2], Alfons Berger[2] and Marco Herwegh[2]

[1]Institut für Geologie, Leibniz Universität Hannover, Germany and [2]Institut für Geologie, Universität Bern, Switzerland

Original Article

Cite this article: Dielforder A, Villa IM, Berger A, and Herwegh M (2023) Tracing wedge-internal deformation by means of strontium isotope systematics of vein carbonates. *Geological Magazine* **159**: 2191–2205. https://doi.org/10.1017/S0016756821001357

Received: 30 July 2021
Revised: 3 December 2021
Accepted: 4 December 2021
First published online: 23 February 2022

Keywords:
accretion; fold-and-thrust belt; mineral veins; fluid flow; strontium isotopes; European Alps

Author for correspondence:
Armin Dielforder,
Email: dielforder@geowi.uni-hannover.de

Abstract

Radiogenic strontium isotopes ($^{87}Sr/^{86}Sr$) of vein carbonates play a central role in the tectono-metamorphic study of fold-and-thrust belts and accretionary wedges and have been used to document fluid sources and fluxes, for example, along major fault zones. In addition, the $^{87}Sr/^{86}Sr$ ratios of vein carbonates can trace the diagenetic to metamorphic evolution of pore fluids in accreted sediments. Here we present $^{87}Sr/^{86}Sr$ ratios of vein carbonates from the Infrahelvetic flysch units of the central European Alps (Glarus Alps, Switzerland), which were accreted to the North Alpine fold-and-thrust belt during the early stages of continental collision. We show that the vein carbonates trace the Sr isotopic evolution of pore fluids from an initial seawater-like signature towards the Sr isotopic composition of the host rock with increasing metamorphic grade. This relationship reflects the progressive equilibration of the pore fluid with the host rock and allows us to constrain the diagenetic to low-grade metamorphic conditions of deformation events, including bedding-parallel shearing, imbricate thrusting, folding, cleavage development, tectonic mélange formation and extension. The strontium isotope systematics of vein carbonates provides new insights into the prograde to early retrograde tectonic evolution of the Alpine fold-and-thrust belt and helps to understand the relative timing of deformation events.

1. Introduction

Deformation at convergent plate margins depends on the presence of fluids and their strength-reducing effect. The build-up of pore fluid overpressures reduces the effective normal stresses, which brings the rock closer to failure and allows deformation at low differential stresses (e.g. Hubbert & Rubey, 1959). Such stress and strength conditions facilitate the formation of mineral veins and are common in fold-and-thrust belts and accretionary wedges (e.g. Fisher & Byrne, 1987; Dahlen, 1990; Labaume *et al.* 1991; Sample & Kopf, 1995; Lacroix *et al.* 2011; Mittempergher *et al.* 2017; Ujiie *et al.* 2018).

Mineral veins are central to studying the tectonometamorphic evolution of convergent margins. From a mechanical perspective, mineral veins provide information on fracture modes, which can be used to constrain fault kinematics and the state of stress during fracturing (e.g. Sibson, 1998; Bons *et al.* 2012). Recently, this aspect has received renewed attention as mineral vein formation in accretionary settings can be linked to stress changes over the earthquake cycle, which allows the constraint of the effective confining pressures (e.g. Sibson, 2013; Takeshita *et al.* 2014; Dielforder *et al.* 2015; Cerchiari *et al.* 2020). From a geochemical perspective, mineral veins can provide information, for example, on fluid sources, fluid–rock interaction, vein formation temperatures and absolute ages of veins (e.g. Vroliijk *et al.* 1988; Sharp & Kirschner, 1995; Tarantola *et al.* 2007; Sample *et al.* 2017; Beaudoin *et al.* 2018).

Over the past decades, vein formation has been successfully studied by stable isotope ($\delta^{13}C$, $\delta^{18}O$) and radiogenic strontium isotope ($^{87}Sr/^{86}Sr$) analysis of vein carbonates (e.g. Dietrich *et al.* 1983; Burkhard *et al.* 1992; McCaig *et al.* 1995; Travé *et al.* 1997; Hilgers & Sindern, 2005; Sample, 2010; Lacroix *et al.* 2011). Stable isotope analysis makes use of the temperature-dependent isotopic fractionation between the fluid and solid (e.g. water–calcite) and can provide information on processes such as the rock-buffering of fluids, carbonate diagenesis or the recrystallization of carbonates during metamorphism (e.g. Burkhard *et al.* 1992; Voigt *et al.* 2015; Sample *et al.* 2017). By comparison, the temperature-dependent isotopic fractionation of Sr is very small, and this small source of bias is eliminated by normalizing $^{87}Sr/^{86}Sr$ ratios to a constant $^{86}Sr/^{88}Sr$ ratio of 0.1194 (Nier, 1938; Krabbenhöft *et al.* 2009). The $^{87}Sr/^{86}Sr$ ratios of vein carbonates and host-rock cements can therefore be used as a tracer. In this respect, the Sr isotope systematics of carbonates has been used to constrain fluid sources, for example, along large thrust faults in the Pyrenees and European Alps and in the foreland of the Rocky Mountains (e.g. Burkhard *et al.* 1992; McCaig *et al.* 1995; Machel *et al.* 1996). These studies

documented the influx of external fluids based on $^{87}Sr/^{86}Sr$ ratios that are clearly distinct from the Sr ratio of the host rock and require an external source.

The $^{87}Sr/^{86}Sr$ ratios of vein carbonates also trace the Sr isotopic evolution of intraformational pore fluids. Fold-and-thrust belts and accretionary wedges typically incorporate calcareous and siliciclastic marine sediments that comprise a mixture of Sr reservoirs. The Sr reservoirs interact with the pore fluid during diagenesis and metamorphism, which might be reflected in the $^{87}Sr/^{86}Sr$ ratios of different generations of veins carbonates. For example, Travé *et al.* (1997) analysed two groups of mineral veins from a small thrust fault developed within Eocene marlstones of the South Pyrenean foreland basin. While the first group of mineral veins showed $^{87}Sr/^{86}Sr$ ratios similar to Eocene seawater, the second group showed more radiogenic (that is, higher) $^{87}Sr/^{86}Sr$ ratios closer to the signature of the host rock. Travé *et al.* (1997) suggested that the difference in the Sr ratios might indicate the evolution of the pore fluid from a seawater-derived fluid towards a diagenetic fluid that interacted with the host rock. However, the impact of external metamorphic fluids could not be excluded. Dielforder *et al.* (2015) analysed three groups of mineral veins that formed successively within marine marlstones of the Alpine fold-and-thrust belt. Similar to the veins from the Pyrenees, the $^{87}Sr/^{86}Sr$ ratios of the three vein groups documented an increase in the Sr ratios from a seawater-like signature towards the isotopic composition of the host rock. Dielforder *et al.* (2015) interpreted this trend to reflect the diagenetic to low-grade metamorphic Sr isotopic evolution of the pore fluid that was essentially undisturbed by external fluids.

The finding that vein carbonates may record a systematic Sr isotopic evolution of pore fluids is promising, because it could help to relate deformation events within the larger-scale diagenetic to low-grade metamorphic evolution of fold-and-thrust belts and accretionary wedges. However, the longer-term and larger-scale isotopic evolution of pore fluids in accretionary settings remains insufficiently understood, also because many studies have focused on specific outcrops and/or distinct tectonic structures. Moreover, the Sr isotopic contrast and interaction between initial seawater-derived fluids, carbonates and the siliciclastic components of accreted sediments has not been systematically explored. The absolute differences in $^{87}Sr/^{86}Sr$ ratios of vein carbonates discussed, for example, by Travé *et al.* (1997) and Dielforder *et al.* (2015) are more subtle than those discussed with respect to the influx of external fluids (e.g. McCaig *et al.* 1995; Machel *et al.* 1996), and may have been overlooked in the past as scatter in a series of values close to host-rock values.

In this study, we address the Sr isotopic systematics of vein carbonates from marine foreland basin sediments of the North Alpine fold-and-thrust belt extending the dataset of Dielforder *et al.* (2015). Our analysis involves several kinds of mineral veins that formed at different stages and in different structural contexts of the prograde to early retrograde tectonometamorphic evolution of the fold-and-thrust belt. In the following, we first provide a geological overview and introduce the different sampling sites located along a 30 km long transect across the fold-and-thrust belt (Section 2 below). Subsequently, we discuss the $^{87}Sr/^{86}Sr$ ratios in terms of pore fluid evolution and in terms of the structural and tectonic evolution of the marine foreland basin sediments (Section 5 below).

2. Geological background

2.a. Geology of the study area

The European Alps are a collisional orogen resulting from the subduction of the Alpine Tethys and the subsequent collision of the Adriatic microplate (upper plate) with southwestern Eurasia ('Europe', lower plate) (e.g. Frisch, 1979; Schmid *et al.* 1996). Continental collision commenced in middle Eocene time with the partial subduction of the European continental margin and associated development of the North Alpine fold-and-thrust belt (e.g. Pfiffner, 1986; Schmid *et al.* 1996; Ford & Lickorish, 2004; Kempf & Pfiffner, 2004; Handy *et al.* 2010).

The study area is located in the central European Alps (Glarus Alps, Switzerland) and provides detailed insights into the evolution of the fold-and-thrust belt, which involved: (1) the Penninic–Austroalpine wedge that formed during the subduction of the Alpine Tethys, (2) the Infrahelvetic flysch units and Subalpine Molasse, (3) the Upper Helvetic nappes, and (4) the European crystalline and sedimentary basement (Fig. 1). The Infrahelvetic flysch units (IFUs) comprise three thrust slices of Upper Cretaceous (Cenomanian–Campanian) to Oligocene passive margin and marine foreland basin sediments, that is, the Ultrahelvetic, South-Helvetic and North-Helvetic flysch units (Milnes & Pfiffner, 1977; Sinclair & Allen, 1992; Jeanbourquin, 1994; Lihou, 1995, 1996*b*) (Fig. 1). These flysch units were scraped off from the subducting European continental margin and accreted in-sequence to the Penninic–Austroalpine wedge (Pfiffner, 1986; Dielforder *et al.* 2016). Remnants of the Upper Penninic sediments are preserved in the northern part of the study area (Fig. 1). The subalpine Molasse comprises shallow marine to continental sediments that were deposited in the foreland basin from middle Oligocene time onwards, when the basin became filled (Sinclair & Allen, 1992). The Molasse sediments were incorporated into the fold-and-thrust belt after the accretion of the IFUs (Pfiffner, 1986; von Hagke *et al.* 2012; Mock *et al.* 2020).

The Upper Helvetic nappes represent the Palaeozoic to Mesozoic sedimentary cover of the European continental margin and were first underthrust and then underplated by duplex accretion to the base of the Alpine wedge. Subsequently, the nappes were thrust along large out-of-sequence thrusts on top of the accreted flysch units and Molasse sediments (see Glarus thrust in Fig. 1c). Thrusting of the Upper Helvetic nappes terminated around late Oligocene to early Miocene time and caused peak metamorphism in the fold-and-thrust belt, which reached zeolite-facies conditions in the north (*c.* 160–180 °C) and sub-greenschist-facies conditions in the south (*c.* 300–350 °C) (Hunziker *et al.* 1986; Pfiffner, 1986; Frey, 1988; Rahn *et al.* 1995; Ebert *et al.* 2007; Lahfid *et al.* 2010; Akker *et al.* 2021*b*). Subsequently, deformation relocated into the crystalline basement, which initiated the exhumation of the Aar massif and the retrograde evolution of the overlying fold-and-thrust belt (Pfiffner, 1986; Burkhard, 1990; Glotzbach *et al.* 2010; Herwegh, *et al.* 2017, 2020; Nibourel *et al.* 2018, 2021). Note that the present-day arcuate geometry of the Glarus thrust evolved during the retrograde evolution of the belt after 20 Ma (Rahn *et al.* 1997) (Fig. 1c).

2.b. Structural evolution of the flysch units and sampling sites

The IFUs constitute a central element of the North Alpine fold-and-thrust-belt and capture the entire collisional evolution from sedimentation in the foreland basin, to accretion, burial, peak metamorphism and exhumation (e.g. Pfiffner, 1986; Lihou, 1996*b*; Sinclair, 1997; Herwegh *et al.* 2008; Dielforder *et al.* 2016). The structural evolution of the IFUs is classically distinguished in three deformation phases that approximately encompass the development during the accretion of the sediments, the emplacement of the Upper Helvetic nappes and the retrograde evolution during

https://doi.org/10.1017/S0016756821001357 Published online by Cambridge University Press

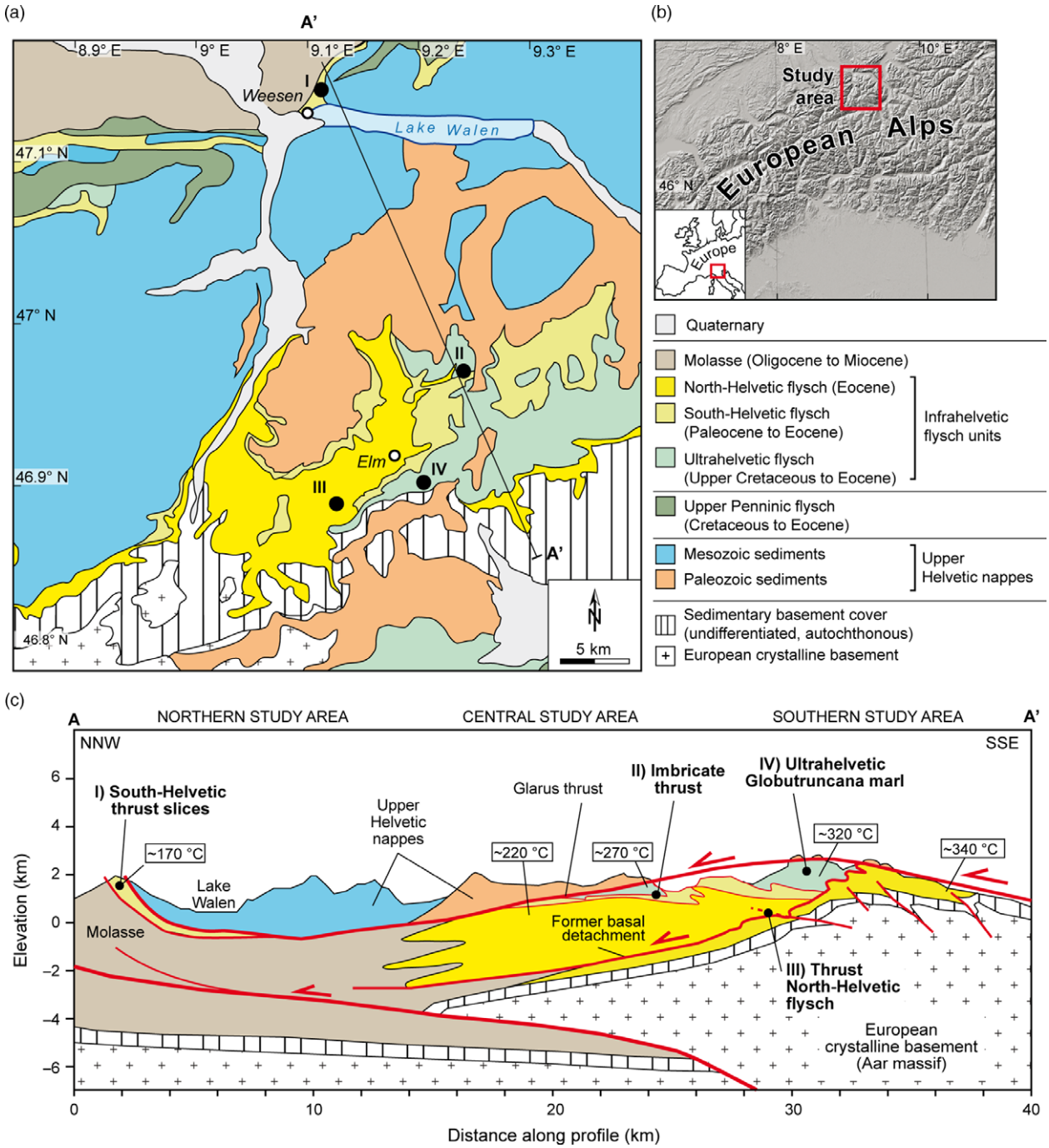

Fig. 1. (a) Geological map of the study area and (b) geographical overview. The line A–A′ indicates the trace of the cross-section shown in (c). (c) Synthetic and simplified cross-section. The approximate sampling sites are indicated together with peak metamorphic temperatures. Temperatures based on Ebert *et al.* (2007), Lahfid *et al.* (2010) and Rahn *et al.* (1995). Geological map in (a) and cross-section in (c) based on Pfiffner (2011).

exhumation, although it should be noted that the deformation phases are diachronous (Schmid, 1975; Milnes & Pfiffner, 1977; Gasser & den Brok, 2008; Dielforder *et al.* 2016). The two main structural elements that occur on a regional scale are a moderately to steeply SE-dipping pressure-solution cleavage and NW-vergent folds. The pressure-solution cleavage is most intensively developed in the central to southern part of the study area, where peak metamorphic temperatures exceeded *c.* 230 °C. This dependency on peak metamorphic temperatures suggests that the pressure-solution cleavage formed mainly during the higher-grade evolution of the IFUs (Dielforder *et al.* 2016; Akker *et al.* 2021*a*). In contrast, folding in the IFUs initiated already during the accretion of the flysch units by particulate flow, when the sediments were only weakly lithified and still deformed as soft sediments, but continued throughout the higher-grade evolution of the IFUs (Gasser & den Brok, 2008; Dielforder *et al.* 2016).

The structural evolution of the IFUs was accompanied by the widespread formation of mineral veins. This includes mineral veins that are structurally linked to distinct tectonic elements such as faults and folds, as well as mineral veins that occur independently from

https://doi.org/10.1017/S0016756821001357 Published online by Cambridge University Press

such elements. In the following, we describe the structural relationships of the mineral veins for the different sampling sites.

2.b.1. Deformation in the Ultrahelvetic flysch unit

The Ultrahelvetic flysch unit was deposited on the most distal part of the European continental margin and was the first flysch unit that was accreted to the Alpine wedge during incipient collision. The unit is folded into isoclinal folds that developed on the metre to hectometre scale (Lihou, 1996*a*,*b*). Peak metamorphic temperatures reached *c.* 320 °C (Ebert *et al.* 2007; Lahfid *et al.* 2010) (Fig. 1c). The Ultrahelvetic flysch unit contains three groups of mineral veins (G_1 to G_3) that also occur in the other flysch units and can be found throughout the central and southern part of the study area (Dielforder *et al.* 2015). The first group of mineral veins (G_1 veins) represents bedding-parallel calcite shear veins that record a top-to-the-NW sense of shear indicating contraction within the flysch units consistent with Alpine shortening directions. G_1 veins are folded together with bedding planes, which indicates that these veins formed before folding (Fig. 2a, b). The second and third groups of mineral veins (G_2 and G_3 veins) comprise quartz-calcite veins, which cross-cut G_1 veins and folds, and that show a mutually cross-cutting relationship with the pressure-solution cleavage, that is, the veins cross-cut the cleavage, but are overprinted by ongoing pressure solution (Fig. 2c–e). G_2 veins form irregular-shaped lenses that can be several decimetres thick and a few metres long, and often comprise centimetre-sized clasts of brecciated host rock. In comparison, G_3 veins form steeply dipping extension fractures that can be several metres long, but are typically thinner than G_2 veins and do not include large clasts of brecciated host rocks. Both G_2 and G_3 veins record brief phases of dilation and extension within the IFUs (Dielforder *et al.* 2015).

Samples of G_1, G_2 and G_3 veins were taken from a *c.* 300 m thick marl unit (Globotruncana marl) with a stratigraphic age of Santonian to Campanian (*c.* 86–72 Ma; Lihou, 1996*a*). The marlstone has a relatively homogeneous composition, although the carbonate content varies locally. In addition to G_1 to G_3 veins, we sampled calcite veins that are structurally linked to folding of the Globotruncana marl. The veins formed in the hinges of isoclinal folds and represent mineralized tension gashes that formed during the final stages of folding (Fig. 2f).

2.b.2. Imbrication of the Ultrahelvetic and South-Helvetic flysch units

The tectonic contacts between the flysch units represent the imbricate thrust faults that were active during accretion (Fig. 1c). The contact between the Ultrahelvetic and the South-Helvetic flysch units is exposed in the central part of the study area, where Ultrahelvetic sandstones are thrust on top of South-Helvetic marlstones (Figs 1c, 3a). The sandstones have a Maastrichtian to Thanetian stratigraphic age (*c.* 72–56 Ma), while the marlstones have a Lutetian to Priabonian stratigraphic age (*c.* 48–34 Ma) (Lihou, 1995, 1996*a*). At the sampling site, the fault plane is defined by a cataclasite that is a few millimetres to centimetres thick. Calcite extension veins occur sporadically directly above the thrust plane, that is, within the lowermost 10 to 20 cm of the hanging wall (Fig. 3b). The veins contain fragments of the cataclasite suggesting that they formed during the activity of the imbricate thrust fault. We further documented steep-dipping calcite extension veins within the uppermost 10 to 15 m of the footwall, which can be some metres long and several centimetres thick (Fig. 3c, d). Some of the extension veins are cut by small thrust faults. The fault planes of these thrusts are partially mineralized by calcite and show a cataclastic reworking of bedding planes, similar to the imbricate thrust. The structural relationship between these smaller thrusts, the calcite extension veins and the imbricate thrust fault is, however, not evident in the field. To better constrain the sequence of formation of these structures, we sampled all kinds of mineralization, comprising the calcite veins from the foot- and hanging wall, as well as the mineralization on the thrust fault surfaces. We further sampled G_1 calcite shear veins and G_3 quartz-calcite extension veins, as well as mineralized fissures (that is, open fractures that are only partially mineralized and exhibit euhedral quartz and calcite crystals; Fig. 3e) from the footwall of the imbricate thrust.

2.b.3. South-Helvetic thrust slice

Thrust slices of South-Helvetic flysch occur in the northernmost part of the study area (Fig. 1a, c). These slices are only a few tens of metres thick and tectonically isolated from the South-Helvetic flysch unit in the central and southern parts of the study area. Peak metamorphic temperatures in the thrust slices reached only 180 –160°C (Rahn *et al.* 1995), which indicates that the slices must have been cut off and thrust towards the north before peak temperatures of *c.* 300 °C were reached in the south. We documented one outcrop within intensively sheared South-Helvetic marlstones of Lutetian to Priabonian age (*c.* 48–34 Ma) near the village of Weesen (Figs 1a, 4). The marls are thrust on top of shallow marine Molasse sediments of Rupelian age (c. 34–28 Ma, lower marine Molasse) and tectonically overlain by Helvetic carbonates of Cenomanian to Turonian age (*c.* 100–90 Ma). Shearing in the marls is recorded by closely spaced anastomosing shear bands that define an intense foliation, which is steeply inclined at present (*c.* 90°; Fig. 4d). Moreover, the marls contain a set of calcite shear veins that formed at a low angle to the foliation (Fig. 4a, d). The veins indicate a sinistral sense of shear and often dip either steeply to the NW or to the SE, which suggests that they represent a set of synthetic Riedel shears. Shear planes within the veins show a tectonic lineation that records former top-to-the-NW thrusting (Dielforder *et al.* 2016) (Fig. 4b). The sheared marlstones further show a typical block-in-matrix fabric, comprising isolated centimetre- to metre-sized intraformational boudins that float within the marlstone matrix (Fig. 4c, d). Some of the boudins are dissected by extensional calcite veins, which formed approximately perpendicular to the shear fabric of the matrix, but are restricted to the boudins. We sampled the calcite shear veins and the extensional veins.

2.b.4. Thrust faulting in the North-Helvetic flysch unit

In the southern part of the study area, the North-Helvetic flysch unit is locally faulted by thrust faults that are hundreds of metres long and have displacements of a few tens of metres. Thrusting was to the NW (Fig. 5). In contrast to the imbricate thrust fault described above (Section 2.b.2), the hanging wall of these thrusts is intensively fractured in the lowermost 2 to 3 m and exhibits a dense network of extension veins, comprising quartz, calcite and minor amounts of chlorite and white mica. The veins overprint well-compacted and cemented host rocks (turbidites), and we interpret them to have formed during the activity of the thrusts (Fig. 5a, b). The veins are locally overprinted by a set of mineralized fissures that formed at a high angle to the extension veins and comprise euhedral quartz and calcite crystals (Fig. 5a, c). We sampled the extension veins and mineralized fissures.

3. Methods

Samples of mineral veins were cleaned, trimmed of weathered surfaces and cut into small blocks. These blocks were crushed, washed

https://doi.org/10.1017/S0016756821001357 Published online by Cambridge University Press

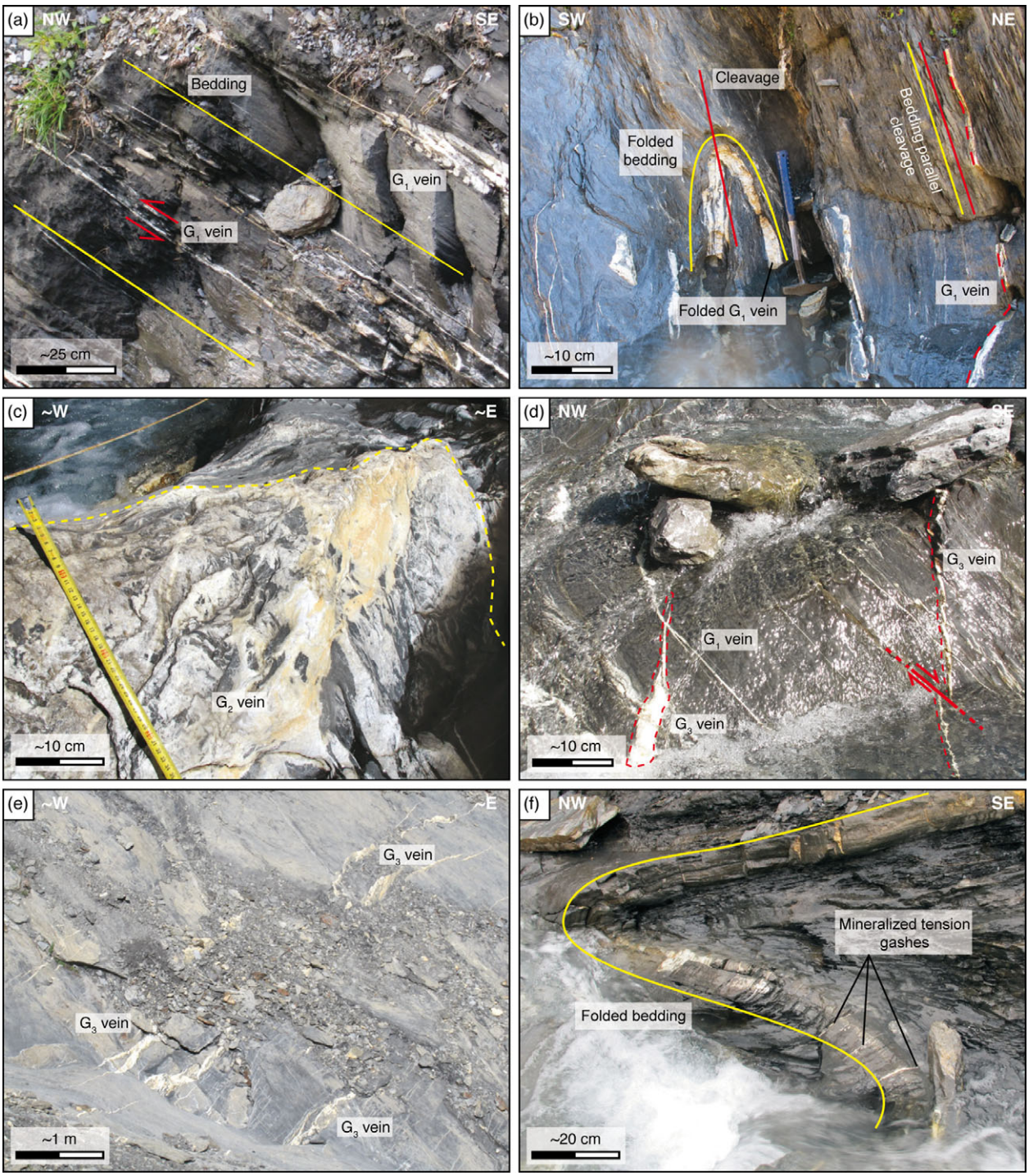

Fig. 2. Examples of mineral veins sampled in the Globotruncana marl of the Ultrahelvetic flysch unit. (a, b) Bedding-parallel G_1 calcite shear veins. G_1 veins were folded together with bedding. (c) G_2 quartz-calcite vein. The vein contains large clasts of brecciated host rock. (d, e) G_3 quartz-calcite extension veins. G_3 veins overprint G_1 veins and the cleavage. (f) Mineralized tension gashes within fold hinges. The tension gashes record a brittle overprint of the folds. Sampling sites: 46.890° N, 9.153° E and 46.874° N, 9.126° E.

and sieved. The 125–250 µm grain fraction was immersed in ethanol and *c.* 100–200 mg of calcite were handpicked under a stereomicroscope. Special care was taken to pick only calcite grains that were devoid of inclusions of host-rock fragments and minerals, such as white mica or chlorite. We further avoided 'sugar-like' agglomerations of fine-grained calcite crystals, as these agglomerates most likely comprise recrystallized calcite. The picked grains were washed in Milli-Q water, cleaned in an ultrasonic bath and dried at room temperature overnight. All calcite samples were dissolved in 1 M HCl.

Sr isotope measurements were performed using a TRITON Plus thermal ionization mass spectrometer (TIMS) (Thermo-Fisher) at the mass spectrometer facility of the Institute of Geological Sciences at the University of Bern. The samples were loaded on rhenium ribbon single filaments in combination with a Ta_2O_5 activator. The measurement commenced when a signal intensity of 5 V on mass

https://doi.org/10.1017/S0016756821001357 Published online by Cambridge University Press

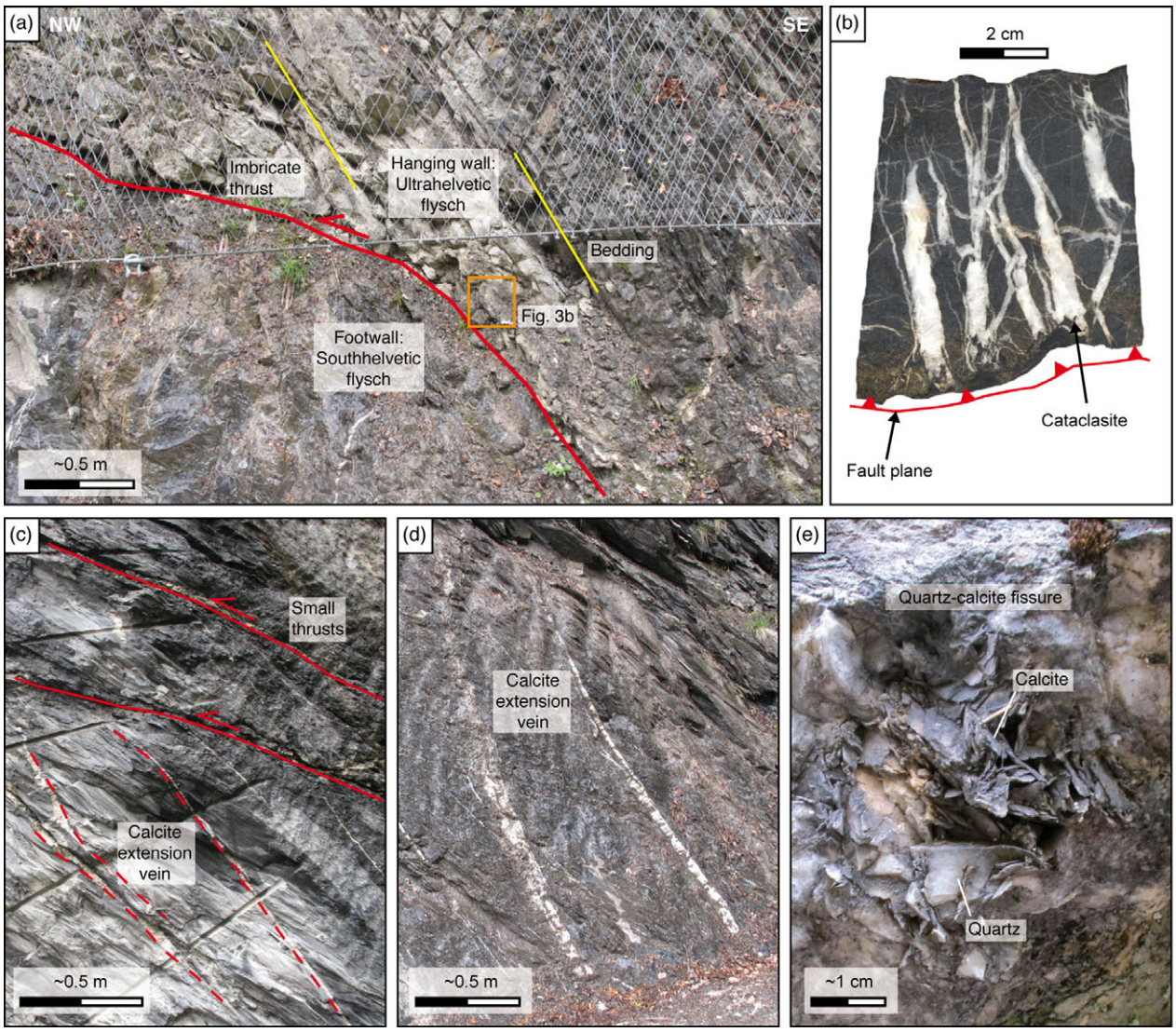

Fig. 3. (a) Tectonic contact between Ultrahelvetic flysch (hanging wall) and South-Helvetic flysch (footwall). (b) Example of calcite extension veins formed in the direct hanging wall of the imbricate thrust fault shown in (a). The veins contain fragments of a cataclasite that formed along the imbricate thrust. (c) Example of small thrusts cross-cutting calcite extension veins in the footwall of the imbricate thrust. (d) Example of steep calcite extension veins in the footwall. (e) Mineralized fissure with euhedral quartz and calcite crystals. Sampling site: 46.9597° N, 9.1881° E.

88 was achieved. The $^{87}Sr/^{86}Sr$ ratios of the samples were normalized to a $^{86}Sr/^{88}Sr$ ratio of 0.1194 (Nier, 1938) using the exponential fractionation law. Samples were also corrected for the offset between the measured $^{87}Sr/^{86}Sr$ value of SRM987 of the individual session and the $^{87}Sr/^{86}Sr$ ratio of 0.71024 (Veizer *et al.* 1999). The external reproducibility (2 s.d.) estimated from the replicate analysis of the standard is ±0.00005 and is taken as uncertainty on the $^{87}Sr/^{86}Sr$ ratios.

4. Results

The $^{87}Sr/^{86}Sr$ ratios obtained for the vein carbonates are illustrated in Figure 6 and listed in online Supplementary Material Table S1. Overall, the $^{87}Sr/^{86}Sr$ ratios fall within the range of *c.* 0.7075 to 0.7095 ($n = 84$). In the following, we report the $^{87}Sr/^{86}Sr$ values obtained for the individual study sites. Note that the $^{87}Sr/^{86}Sr$ ratios of G_1, G_2 and G_3 veins in the Ultrahelvetic flysch units were originally reported by Dielforder *et al.* (2015) and are replicated here for convenience.

Ultrahelvetic Flysch Unit (Fig. 6a). The $^{87}Sr/^{86}Sr$ ratios of vein carbonate from G_1 calcite shear veins range between 0.7075 and 0.7079 ($n = 13$). For comparison, the vein carbonates from G_2 and G_3 quartz-calcite veins show more radiogenic $^{87}Sr/^{86}Sr$ ratios of 0.7080–0.7086 ($n = 12$) and 0.7081–0.7089 ($n = 12$), respectively. The vein carbonates of tension gashes preserved in the hinges of folds have $^{87}Sr/^{86}Sr$ ratios between 0.7082 and 0.7086 ($n = 4$), and overlap with the values obtained for G_2 and G_3 veins.

Imbricate Thrust Fault (Fig. 6b). The vein carbonates from the calcite extension veins in the hanging wall directly above the imbricate thrust fault have $^{87}Sr/^{86}Sr$ ratios that fall within a narrow range of 0.7082 to 0.7083 ($n = 4$). Similar values of *c.* 0.7082 to 0.7083 were obtained for the calcite extension veins ($n = 2$) and the small thrusts in the footwall ($n = 2$), respectively. For comparison, the G_1 calcite shear veins in the footwall show slightly lower $^{87}Sr/^{86}Sr$ ratios of 0.7080–0.7081 ($n = 2$), while the G_3 quartz-calcite veins have more radiogenic $^{87}Sr/^{86}Sr$ values of 0.7084–0.7086 ($n = 3$). Finally, calcite crystals from the fissures preserved in the footwall show $^{87}Sr/^{86}Sr$ ratios of 0.7091 to 0.7095 ($n = 3$).

https://doi.org/10.1017/S0016756821001357 Published online by Cambridge University Press

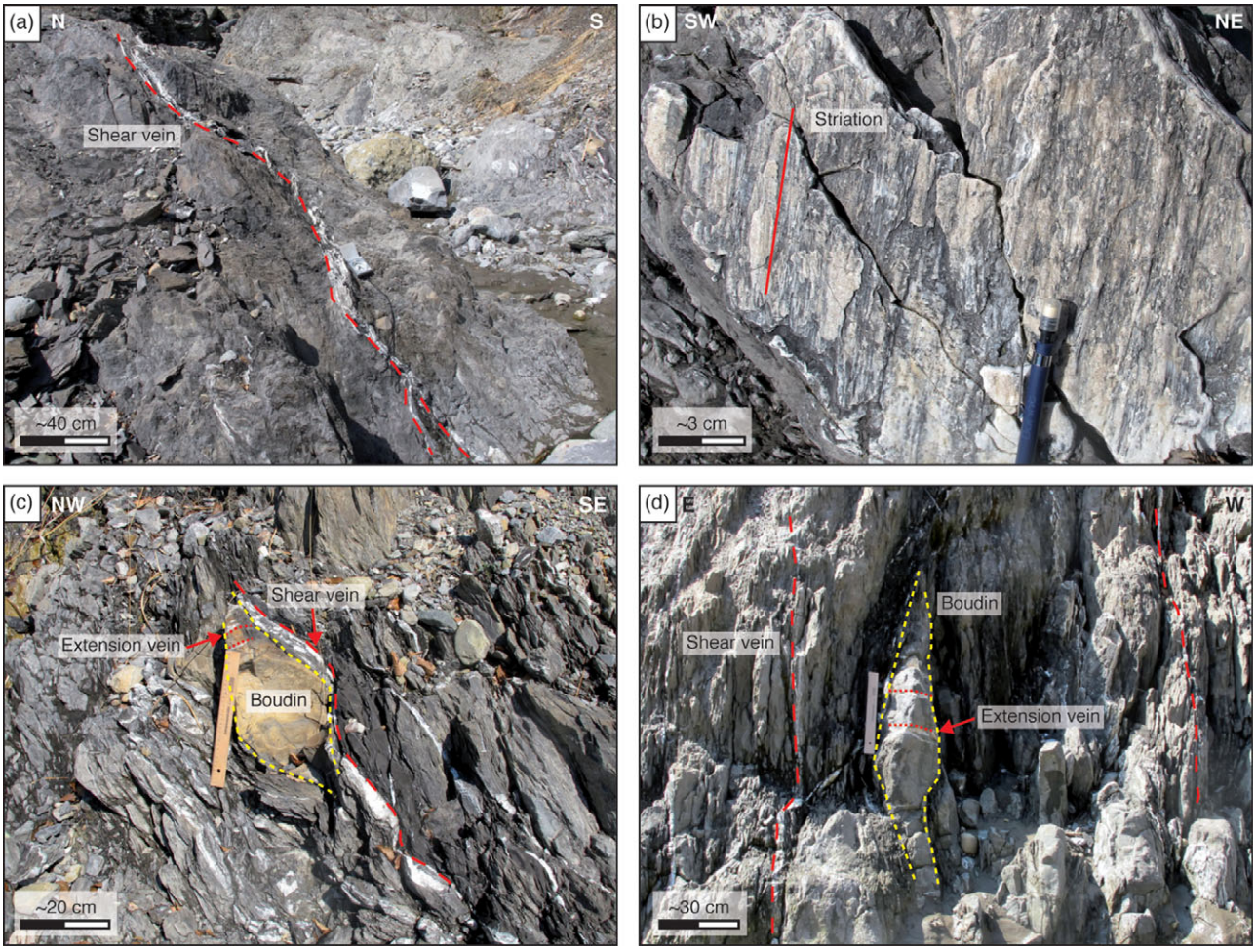

Fig. 4. South-Helvetic thrust slice exposed in northernmost part of the study area. (a) The marl is intensively sheared and comprises long shear veins. (b) Striations (*c.* 130|45) on shear surfaces indicate top-to-NW shearing (cf. Dielforder *et al.* 2016). (c, d) Examples of boudins dissected by calcite extension veins. Sampling site: 47.1407° N, 9.1073° E.

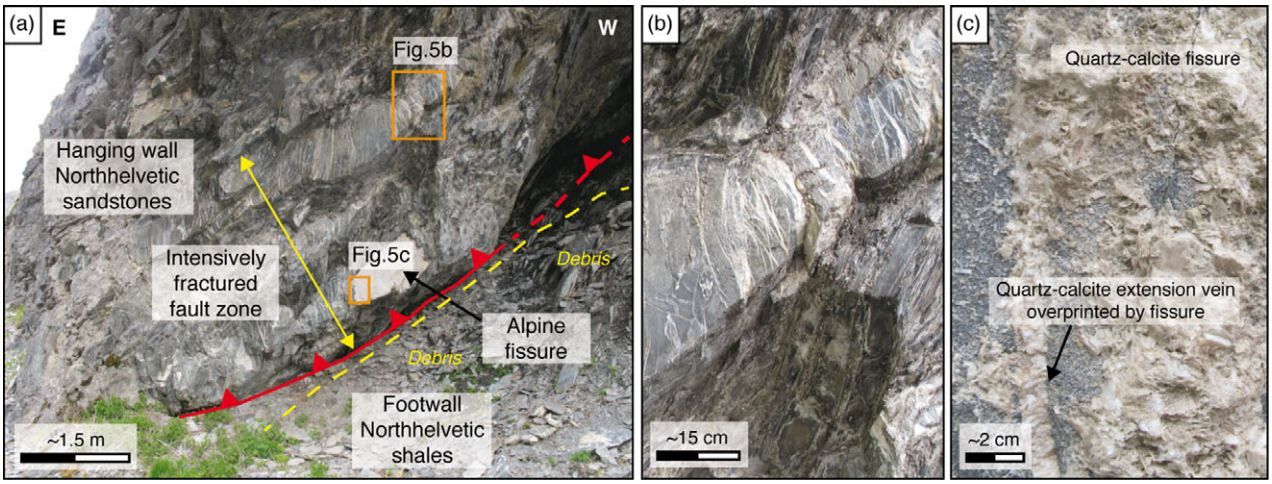

Fig. 5. (a) Thrust fault in North-Helvetic flysch. The hanging wall of the thrust is intensively fractured. The mineral veins comprise quartz, calcite and minor amounts of chlorite and white mica. (b) Detail of mineral veins within the hanging wall of the thrust shown in (a). The veins overprint well-compacted and foliated rocks. (c) Detail of retrograde fissure overprinting the fault structure and related extension veins. Sampling site: 46.8877° N, 9.1273° E.

https://doi.org/10.1017/S0016756821001357 Published online by Cambridge University Press

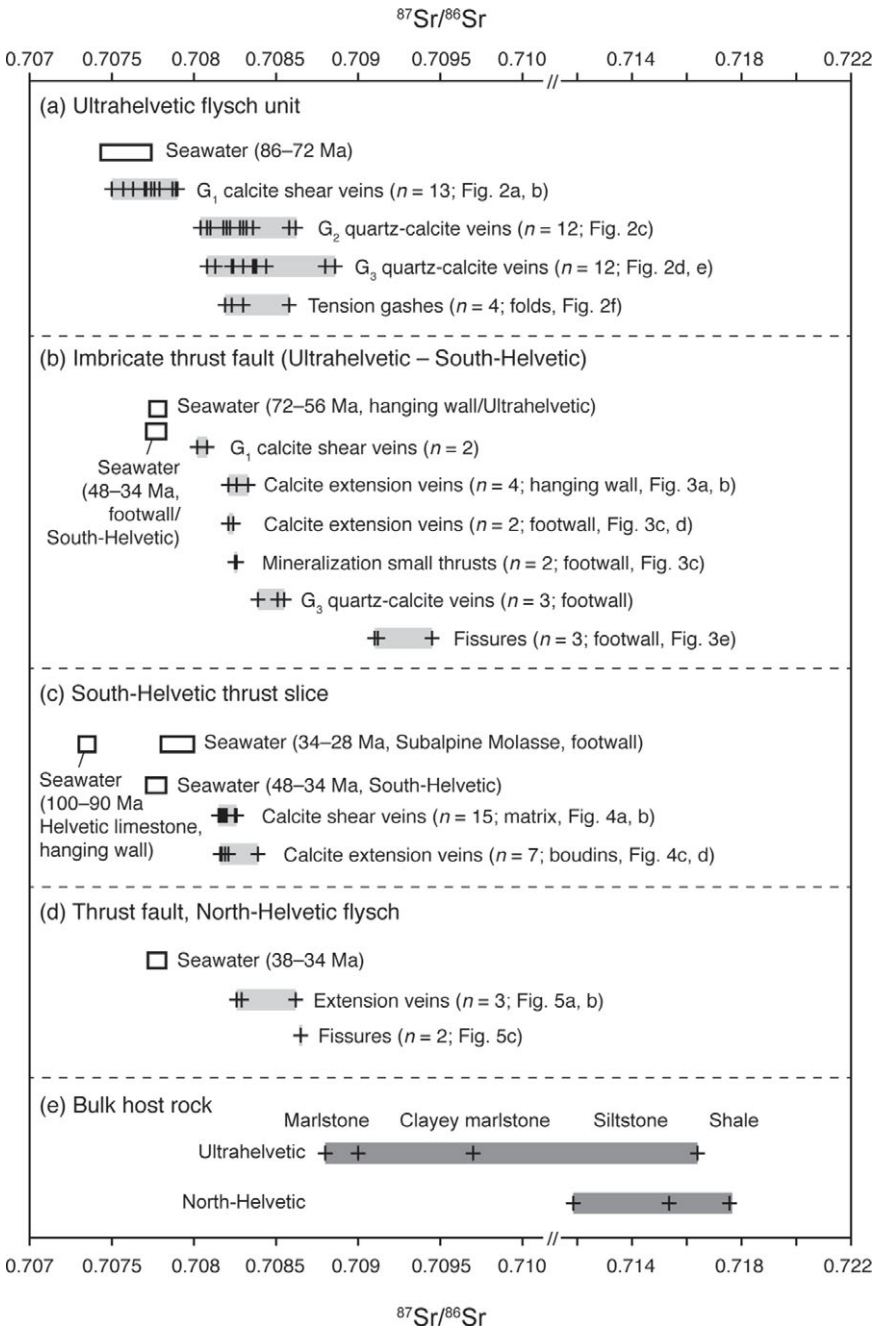

Fig. 6. Sr isotopic composition of vein carbonates (crosses) grouped for the different vein generations and sampling sites (a–d). Note the change in scale for $^{87}Sr/^{86}Sr$ values >0.71. See Figures 2–5 for examples of analysed mineral veins. The 2σ uncertainties on the $^{87}Sr/^{86}Sr$ ratios of vein carbonates are smaller than the symbols. Sr ratios of G_1, G_2 and G_3 veins in (a) from Dielforder *et al.* (2015). Seawater values at the time of sediment deposition are shown for comparison; data from McArthur *et al.* (2001). Bulk host-rock values in (e) are recalculated to the time of metamorphism at 25 Ma; data compiled from Dielforder *et al.* (2015) and Hilgers & Sindern (2005).

South-Helvetic Thrust Slice (Fig. 6c). The vein carbonates from the shear veins in the marlstone matrix have $^{87}Sr/^{86}Sr$ ratios that fall within a narrow range of 0.7082 to 0.7083 ($n = 15$). Similar values of *c.* 0.7082 to 0.7084 were obtained for the extension veins from the boudins ($n = 7$).

Thrust Fault, North-Helvetic Flysch (Fig. 6d). The vein carbonates from the extension veins in the hanging wall directly above the thrust fault have $^{87}Sr/^{86}Sr$ ratios between 0.7083 and 0.7086 ($n = 3$). Slightly higher values of *c.* 0.7087 were obtained for the fissures overprinting the extension veins ($n = 2$).

5. Discussion

Figure 6 shows the $^{87}Sr/^{86}Sr$ ratios of vein carbonate together with the $^{87}Sr/^{86}Sr$ ratio of seawater (McArthur *et al.* 2001) at the time of sediment deposition and the $^{87}Sr/^{86}Sr$ ratios of samples of Ultrahelvetic and North-Helvetic host rocks. The host-rock values are compiled from the literature and back-calculated to 25 Ma, that is, the approximate time of metamorphism in the IFUs (Hunziker *et al.* 1986; Hilgers & Sindern, 2005; Dielforder *et al.* 2015; Akker *et al.* 2021*b*). The host-rock values are listed in online Supplementary Material Table S2. Overall, the $^{87}Sr/^{86}Sr$ ratios of vein carbonate plot between the seawater values and the host-rock values. In more detail, we find that the $^{87}Sr/^{86}Sr$ ratios of vein carbonate correlate with the relative age of the mineral veins, where more radiogenic isotope ratios tend to be associated with mineral veins that formed at a later stage of the structural evolution. This relationship is best expressed by the Sr isotope systematics of the G_1 to G_3 veins and mineralized fissures, as discussed in the following section. The $^{87}Sr/^{86}Sr$ ratios of all other vein carbonates are subsequently discussed in Section 5.b below.

https://doi.org/10.1017/S0016756821001357 Published online by Cambridge University Press

5.a. Strontium isotope ratios and pore fluid evolution

G_1 veins formed during the earliest structural evolution of the IFUs and are overprinted by all other structural elements, including folds, the pressure-solution cleavage and other mineral veins (Dielforder *et al.* 2015, 2016) (Fig. 2a, b, d). The Sr isotope ratios of G_1 veins are the lowest ratios obtained for all samples and generally closest to the Sr isotope ratios of seawater at the time of sediment deposition (Fig. 6a, b). For the Ultrahelvetic flysch unit, the $^{87}Sr/^{86}Sr$ ratios of G_1 veins partly overlap with the seawater values. By comparison, G_2 and G_3 veins formed after G_1 veins and show more radiogenic $^{87}Sr/^{86}Sr$ ratios that range between the values of G_1 veins and the host rocks (Fig. 6a). Finally, we find that the mineralized fissures, which record the latest stages of vein formation in the IFUs, show the most radiogenic $^{87}Sr/^{86}Sr$ ratios of all vein carbonates. In detail, the three fissures sampled in the footwall of the imbricate thrust fault that emplaced the Ultrahelvetic flysch on the South-Helvetic flysch show $^{87}Sr/^{86}Sr$ ratios that overlap with the range of host-rock values and are distinctly higher than the values of nearby G_3 veins (Fig. 6b). Similarly, the $^{87}Sr/^{86}Sr$ ratios of the two fissures sampled along the thrust fault in the North-Helvetic flysch show the highest values obtained for this outcrop (Fig. 6d). Taken together, the Sr isotope ratios of G_1 to G_3 veins and mineralized fissures indicate an overall increase in $^{87}Sr/^{86}Sr$ ratios of vein carbonate with the structural evolution of the IFUs, from a seawater-like signature towards the signature of the host rock. We interpret this trend to reflect the diagenetic to metamorphic evolution of pore fluids within the IFUs, as outlined in the following.

The IFUs were deposited on the rifted continental margin of Europe and consisted of biogenic marine carbonates and terrigenous sediments comprising quartz, micas, clays, alkali-feldspars and plagioclase (Frey, 1988; Tarantola *et al.* 2007, 2009; Dielforder *et al.* 2015; Mullis *et al.* 2017; Akker *et al.* 2021*b*). At the time of sedimentation, the initial pore fluid derived from seawater and thus had a similar $^{87}Sr/^{86}Sr$ ratio. Likewise, the carbonates consisting of skeletal remnants of marine organisms had a Sr isotopic composition similar to the one of contemporaneous seawater (Milliman, 1974; Dielforder *et al.* 2015; El Meknassi *et al.* 2018). In contrast, the terrigenous components had a Sr isotopic composition that was on average more radiogenic than the one of seawater (Fig. 6e). Accordingly, the bulk Sr isotopic composition of the flysch sediments varies with the carbonate and silicate content, such that marlstones show less radiogenic Sr ratios than siltstones and shales (Fig. 6e). We further find that the range of $^{87}Sr/^{86}Sr$ ratios is similar for Ultrahelvetic and North-Helvetic siltstones and shales, which suggests that the Sr isotopic signature of the terrigenous components remained similar throughout the deposition of the three flysch units. In more detail, the Sr isotopic composition of the terrigenous components will have differed for the individual mineral phases. In particular, rubidium-bearing silicates, such as alkali-feldspars, illite, muscovite or biotite, inherited from old continental crust typically contain radiogenic Sr, due to the beta decay of ^{87}Rb to ^{87}Sr (McLennan *et al.* 1990; Clauer & Chaudhuri, 1995). Thus, the elevated $^{87}Sr/^{86}Sr$ ratios of the host rocks should mainly come from the sheet silicates and feldspars. In summary, the initial pore fluid was not in isotopic equilibrium with the bulk sediments after the deposition of the IFUs.

With the onset of diagenesis and related sediment alteration, the pore fluid in the IFUs evolved. Microstructural observations from the IFUs indicate that the earliest tectonic deformation affected soft sediments, which suggests that diagenesis occurred mainly syntectonically during incorporation of the flysch units into the Alpine wedge (Dielforder *et al.* 2016). The early diagenetic alteration of calcareous sediments includes the recrystallization of biogenic calcite to secondary calcite (Milliman, 1974; Elderfield *et al.* 1982). Carbonate diagenesis typically takes place at temperatures below 100 °C and involves the release of Sr into the pore fluid from the biogenic carbonates, whose Sr concentration is one to three orders of magnitude higher than in seawater (Richter & Liang, 1993; Fantle & DePaolo, 2006; Voigt *et al.* 2015). The Sr release buffers the isotopic composition of the pore fluid during carbonate diagenesis. We therefore suggest that the seawater-like $^{87}Sr/^{86}Sr$ ratios of G_1 veins record a formation of these veins during carbonate diagenesis and early tectonic burial.

Another early diagenetic process is the transformation of smectite to illite, which occurs between 80 and 150 °C in most geological settings (Pytte & Reynolds, 1989; Awwiller, 1993; Moore & Saffer, 2001). Although young authigenic smectites may lack relevant amounts of radiogenic ^{87}Sr, the smectite-to-illite transformation is accompanied by alkali-feldspar albitization, which releases Sr with elevated $^{87}Sr/^{86}Sr$ ratios into the pore fluid (Awwiller, 1993; Baccar *et al.* 1993; Clauer *et al.* 2020). Additionally, the recrystallization of detrital mixed-layer illite-smectite is likely to release more ^{87}Sr into the pore fluid. We therefore expect that the Sr isotopic signature of the pore fluid becomes more radiogenic during the smectite-to-illite transformation. It remains difficult to quantify the change in Sr isotopic composition, which would require detailed information on fluid volumes, fluid fluxes, Sr concentrations and isotope ratios, but the process may be constrained for the IFUs by the following considerations. First, sediment compaction within the upper 4 to 5 km of accretionary wedges results in a strong reduction in porosity and expulsion of pore fluids (e.g. Wang, 1994; Moore & Saffer, 2001). Dielforder *et al.* (2016) modelled the compaction and diagenetic fluid release for the IFUs and found that the smectite-to-illite transformation occurred after the main compaction of the sediments, when much of the initial pore fluid was already expelled. This suggests that the smectite-to-illite transformation and related fluid liberation resulted in a substantial alteration of the initial pore fluid. Second, the formation temperatures of G_2 and G_3 quartz-calcite veins from the Ultrahelvetic flysch unit have been previously constrained by oxygen isotope thermometry to *c.* 210–290 °C (Dielforder *et al.* 2015) (Fig. 7). Thus, the quartz-calcite veins formed after the smectite-to-illite transformation, which suggests that vein carbonates with $^{87}Sr/^{86}Sr$ ratios lower than those of G_2 and G_3 veins but higher than those for seawater reflect the approximate Sr isotopic signature of the pore fluid during illitization.

After the smectite-to-illite transformation, the Sr isotopic composition of the pore fluid continued to develop towards the signature of the host rock, as illustrated by the $^{87}Sr/^{86}Sr$ ratios of G_2 and G_3 veins from the Ultrahelvetic flysch unit, which increase with the vein formation temperature (Dielforder *et al.* 2015) (Fig. 7). This development towards more radiogenic values could in principle reflect two processes: the release of Sr into the pore fluid due to continuous recrystallization of minerals (e.g. Glodny *et al.* 2008), and temperature-dependent diffusion of Sr (e.g. Dodson, 1973). Because of the high Ar and Sr retentivity of micas (Villa, 1998) and because the dissolution-reprecipitation rate at 200 °C is around ten orders of magnitude faster than volume diffusion (Villa, 2016), we are forced to conclude that the increase in the $^{87}Sr/^{86}Sr$ ratios was not primarily controlled by Sr diffusion. In contrast, the recrystallization of micas at low-grade metamorphic conditions is well documented also for the flysch units. Akker *et al.* (2021*a*, *b*) showed that the development of the pressure-solution

https://doi.org/10.1017/S0016756821001357 Published online by Cambridge University Press

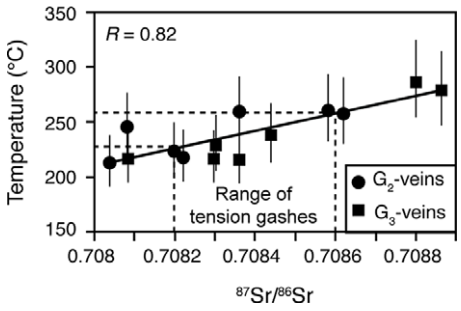

Fig. 7. Diagram showing the positive correlation between the $^{87}Sr/^{86}Sr$ ratios of G_2 and G_3 veins from the Ultrahelvetic flysch unit and the formation temperature of these veins as constrained by oxygen isotope thermometry (data from Dielforder *et al.* 2015). *R* is the correlation coefficient. The range of $^{87}Sr/^{86}Sr$ ratios obtained for nearby tension gashes overlaps with the values of G_2 and G_3 veins, which suggests an approximate formation temperature of 230–260 °C for the tension gashes as indicated by dashed lines. See Section 5.b.1 for details.

cleavage in the IFUs at temperatures above 230 °C involved the partial recrystallization of white micas. Tarantola *et al.* (2007, 2009) documented the chloritization of detrital biotites in the North-Helvetic flysch at temperatures of *c.* 270 °C. After the smectite-illite transformation and temperatures above 200 °C, illite is successively transformed into muscovite (Hunziker *et al.* 1986; van de Kamp, 2008). We therefore argue that the increase in $^{87}Sr/^{86}Sr$ ratios primarily reflects a release of ^{87}Sr into the pore fluid due to the recrystallization of minerals and associated mass transfer processes.

Taken together, the diagenetic and low-grade metamorphic processes discussed above contributed to the Sr isotopic equilibration of the flysch units. Recently, Akker *et al.* (2021*b*) evaluated the grain-size dependent isotopic resetting of the K–Ar system for white micas from the IFUs and found that the system is only partially reset, except for the southernmost part of the study area ($T_{max} \approx 330$ °C), where the grain-size fraction of ≤0.8 μm is nearly reset. We therefore propose that the Rb–Sr system was also only partially reset and that the late-stage Sr isotopic evolution of the pore fluid was dominated by the interaction with silicates rather than with the bulk rock, which would have required a higher metamorphic grade and full recrystallization of the sediments. Independently, the bulk Sr isotopic evolution of the pore fluid reflects the progressive isotopic equilibration and is recorded by the vein carbonates. It is important to note that the pore fluid evolution was not synchronous within the different flysch units, as the flysch units were accreted successively to the Alpine wedge (that is, the Ultrahelvetic flysch unit was already accreted and experienced syntectonic diagenesis, while the North-Helvetic flysch was still being deposited in the foreland basin). Moreover, the detailed Sr isotopic evolution will have varied between the units and on smaller spatial scales, owing to differences in the initial Sr isotopic composition of seawater and sediments (Fig. 6). The absolute $^{87}Sr/^{86}Sr$ values of vein carbonates from different units can therefore not be directly compared. Likewise, small differences in the $^{87}Sr/^{86}Sr$ ratio of nearby mineral veins do not necessarily reflect the sequence of vein formation, as evident from the scatter in Figure 7. Independent of these restrictions, the overall Sr isotope systematics of the vein carbonates allow us to constrain the approximate diagenetic to low-grade metamorphic conditions of vein formation and can therefore allow a better understanding of aspects of the structural and tectonic evolution, as discussed in the following section.

5.b. Implications for the structural and tectonic evolution of the Infrahelvetic flysch units

In addition to the G_1 to G_3 veins and mineralized fissures discussed in the previous section, we sampled mineral veins that relate to distinct structural and tectonic features (Section 2.b above) and help to understand their genesis and sequence of formation.

5.b.1. Folding

The tension gashes in the hinge zone of isoclinal folds in the Ultrahelvetic flysch unit document a brittle overprint of the folds and thus formed after or during the latest stage of folding. The vein carbonates from the tension gashes have $^{87}Sr/^{86}Sr$ ratios that overlap with Sr ratios of nearby G_2 and G_3 veins, which indicates that the gashes and veins formed at similar diagenetic-metamorphic conditions (Fig. 6a). In addition, the $^{87}Sr/^{86}Sr$ ratios of the G_2 and G_3 veins exhibit a strong positive correlation with the vein formation temperatures and increase from *c.* 0.7080 and 210 °C to *c.* 0.7089 and 290 °C (Dielforder *et al.* 2015) (Fig. 7). Transferred to the $^{87}Sr/^{86}Sr$ ratios obtained for the tension gashes, this correlation between the Sr ratios and temperature suggests that the tension gashes formed at *c.* 230–260 °C (Fig. 7). This finding is consistent with the structural constraints, which indicate that folding in the IFUs initiated during the early structural evolution and at temperatures below 160 °C, and that the folds were subsequently tightened and overprinted by the pressure-solution cleavage, which mainly developed above 230 °C (Dielforder *et al.* 2016). Instead, the classical interpretation was that folding and cleavage development in the IFUs represent one (and the main) deformation event (e.g. Schmid, 1975; Milnes & Pfiffner, 1977).

5.b.2. Imbricate thrusting

The calcite extension veins that formed in the immediate hanging wall of the imbricate thrust emplacing the Ultrahelvetic flysch on the South-Helvetic flysch have similar $^{87}Sr/^{86}Sr$ ratios as the vein carbonate from the extension vein and the small thrusts in the footwall of the imbricate fault (Fig. 6b). This relationship suggests that the structures formed at similar times and that the small thrusts may represent splays from the main fault. Likewise, the calcite extension veins in the footwall may record damage in the surrounding of the imbricate thrust. Notably, all $^{87}Sr/^{86}Sr$ ratios of vein carbonate related to imbrication are more radiogenic than the Sr ratios of nearby G_1 veins, which suggests that the G_1 veins record shearing before imbrication (Fig. 6b). Moreover, the $^{87}Sr/^{86}Sr$ ratios are distinctly more radiogenic than seawater at the time of sedimentation (note that the seawater values are similar for the sediments in the hanging wall and footwall despite their different ages; Fig. 6b), but less radiogenic than the $^{87}Sr/^{86}Sr$ ratios of nearby G_3 quartz-calcite veins and mineralized fissures. Thus, the Sr ratios suggest that the imbrication of the units occurred at *c.* 100–150 °C, that is, after carbonate diagenesis but before quartz cementation, which typically becomes active in accretionary settings at 150–200 °C (e.g. Moore *et al.* 2007). This temperature constraint is consistent with the cataclasis along the thrust faults and the off-fault damage, which both suggest that the rocks were already consolidated and had some elastic strength during faulting (e.g. Sibson, 1977; Fagereng & Toy, 2011).

5.b.3. South-Helvetic thrust slice

Vein carbonates from the South-Helvetic thrust slice preserved in the northernmost part of the study area document similar $^{87}Sr/^{86}Sr$ ratios for the calcite shear veins and the calcite extension veins

https://doi.org/10.1017/S0016756821001357 Published online by Cambridge University Press

dissecting the boudins (Fig. 6c). We interpret these Sr ratios to indicate that the shearing and formation of the tectonic mélange occurred simultaneously and was related to the transport of the thrust slice, which agrees with concepts for mélange formation within shear zones (Remitti *et al.* 2007; Fagereng & Sibson, 2010; Festa *et al.* 2010). Interestingly, the veins in the South-Helvetic thrust slice have similar Sr ratios to vein carbonates related to imbricate thrusting at the Ultrahelvetic flysch – South-Helvetic flysch contact. As the sediments in the thrust slice have a similar age and composition to the sediments in the footwall of the imbricate thrust (Lihou, 1995, 1996*a*), we expect that the pore fluid evolution was similar for both localities. The similarity in the Sr ratios therefore suggests that both imbricate thrusting and the tectonic transport of the South-Helvetic thrust slice occurred at diagenetic conditions, which is consistent with the peak temperatures of *c.* 160–180 °C inferred for the South-Helvetic thrust slice (Rahn *et al.* 1995).

5.b.4. Late-stage thrust faulting

Vein carbonates from the thrust fault in the North-Helvetic flysch show elevated $^{87}Sr/^{86}Sr$ ratios (Fig. 6d). In detail, the Sr ratios of the mineralized fissures are slightly more radiogenic than the Sr ratios of the quartz-calcite extension veins that are overprinted by the fissures, which is consistent with the general pore fluid evolution towards a more radiogenic signature. The radiogenic signature of the vein carbonates suggests that the thrust was active at or close to peak metamorphic conditions, which would be consistent with structural constraints indicating that the thrust overprints well-compacted and foliated rocks (Dielforder *et al.* 2016). The intriguing aspect of this activity is that the thrust documents late-stage frictional faulting in the North-Helvetic flysch. The activity of the thrust may therefore be related to the relocation of the deformation into the crystalline basement of the Aar massif and faulting near the basement–cover contact (Pfiffner, 1986; Nibourel *et al.* 2021) (Fig. 1). In this case, thrust faulting took place during the earliest retrograde evolution of the IFUs and was potentially related to the early doming and exhumation of the Aar massif.

5.c. External fluids

We interpret the trend in the $^{87}Sr/^{86}Sr$ ratios of vein carbonates to document the diagenetic to metamorphic evolution of the pore fluid due to local fluid–rock interaction. This pore fluid evolution could have been disturbed by an influx of external fluids with a different Sr isotopic composition.

In fold-and-thrust belts and accretionary wedges, external fluids can migrate along major faults, including the decollement or megathrust, and major splay faults such as imbricate or out-of-sequence thrusts (McCaig *et al.* 1995; Machel *et al.* 1996; Travé *et al.* 1997; Lauer & Saffer, 2015; Cerchiari *et al.* 2020). Fluid flow along the Glarus thrust has been studied by means of radiogenic Sr isotope and stable isotope ($\delta^{13}C$, $\delta^{18}O$) systematics (Burkhard *et al.* 1992; Abart *et al.* 2002; Badertscher *et al.* 2002). These studies inferred a syntectonic flow of external, basement-derived metamorphic fluids along the Glarus thrust for the southernmost part of the study area, where the thrust overlies Mesozoic marine carbonates. The metamorphic fluid has been related to high $^{87}Sr/^{86}Sr$ ratios of >0.71 recorded in calcmylonites that formed along the thrust plane. In addition, fluid infiltration into the uppermost metres of the footwall caused significant ^{18}O depletion in the limestones. In contrast, where the Glarus thrust overlies flysch sediments, fluid flow along the thrust was found to be consistent with fluids sourced from the flysch units, suggesting that there was a net flux of fluids from the flysch towards the Glarus thrust (Burkhard *et al.* 1992; Abart *et al.* 2002; Badertscher *et al.* 2002). This finding is consistent with the stable isotope systematics of calcite cements and vein carbonates from the Ultrahelvetic flysch unit, which indicate that the calcite cements bear a marine equilibrated stable isotope signature, and that the vein carbonates precipitated from a local, rock-buffered fluid (Dielforder *et al.* 2015). It has been further shown that the deuterium isotope values of fluid inclusions in quartz from mineralized fissures from the North-Helvetic flysch unit are in equilibrium with sheet silicates of the host rocks and that the fluid inclusions contain locally sourced methane (Tarantola *et al.* 2007; Mangenot *et al.* 2021) These findings also indicate vein precipitation from a rock-buffered fluid. We therefore suppose that the $^{87}Sr/^{86}Sr$ ratios of vein carbonates reported in this study do not record external fluids that infiltrated from the Glarus thrust into the flysch units.

The imbricate thrust emplacing the Ultrahelvetic flysch on the South-Helvetic flysch likely rooted in the decollement and may have channelled diagenetic to metamorphic fluids migrating upwards along the basal fault (e.g. Machel *et al.* 1996; Lauer & Saffer, 2015; Cerchiari *et al.* 2020). The $^{87}Sr/^{86}Sr$ ratios of vein carbonates related to imbricate thrusting are much less radiogenic than the values obtained, for example, by Burkhard *et al.* (1992) for the calcmylonites. We therefore exclude that the imbricate thrust channelled relevant amounts of metamorphic fluids. On the other hand, migrating diagenetic fluids may have had Sr ratios similar to the one recorded in the vein carbonates, as the decollement was located within flysch sediments of similar composition and stratigraphic age (Pfiffner, 1986). We can therefore not exclude the migration of nearby diagenetic fluids along the imbricate thrust. Independently, the general increase towards more radiogenic Sr ratios documented by the different vein generations that formed before (G_1 veins) and after imbricate thrusting (G_3 veins, fissures) would still reflect the overall diagenetic to metamorphic evolution of the pore fluid, similar to the development in the Ultrahelvetic flysch.

The thrust slice of South-Helvetic marls in the northern part of the study area is tectonically intercalated between Oligocene Molasse sediments and Upper Cretaceous marine limestones, providing both units as potential sources for external fluids. Fluids derived from the Cretaceous limestones in the hanging wall must be expected to show $^{87}Sr/^{86}Sr$ ratios close to the one of contemporaneous seawater, that is, *c.* 0.7073–0.7074 (McArthur *et al.* 2001). The values are significantly lower than for contemporaneous seawater of the South-Helvetic marls (Fig. 6c). A significant influx of fluids from the Cretaceous limestone should therefore result in low $^{87}Sr/^{86}Sr$ ratios, which is not recorded in the Sr isotopes of the mineral veins. We therefore exclude the limestones as the fluid source. In contrast, the $^{87}Sr/^{86}Sr$ ratios of seawater during the deposition of the shallow marine Molasse sediments are only slightly higher and partly overlap with the one for the South-Helvetic marls (Fig. 6c). An influx of diagenetic fluids from the Molasse sediments may therefore be difficult to detect in the Sr ratios of vein carbonates. However, the shearing and mélange formation should have mainly occurred during the tectonic transport of the thrust slice and before its emplacement on the Molasse sediments. We therefore exclude fluids expelled from the Molasse as a relevant source for the vein carbonates.

https://doi.org/10.1017/S0016756821001357 Published online by Cambridge University Press

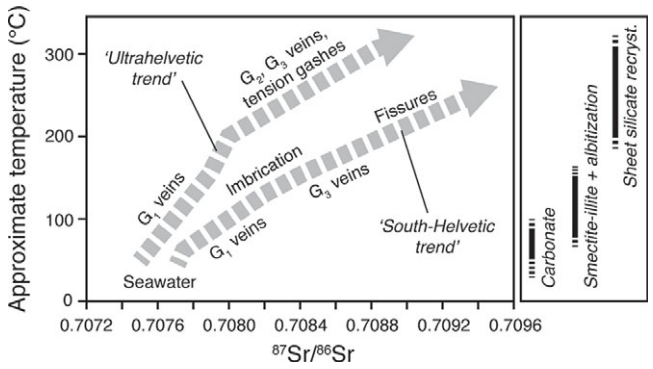

Fig. 8. Diagram illustrating the Sr isotopic evolution of pore fluids in the Ultrahelvetic flysch and South-Helvetic flysch units. The increase from the seawater-like signature towards more radiogenic values is interpreted to relate to diagenetic and metamorphic processes, including carbonate diagenesis, smectite-to-illite transformation, alkali-feldspar albitization, illite-to-muscovite transformation and recrystallization (recryst.) of detrital white mica and biotite. See Sections 5.a and 6 for details.

6. Summary and conclusions

The $^{87}Sr/^{86}Sr$ ratios of vein carbonates from the IFUs indicate a consistent increase from a seawater-like signature recorded by early veins towards the signature of the host rock recorded by late veins. We interpret these values as tracing the bulk diagenetic to low-grade metamorphic pore fluid evolution, which was governed by carbonate diagenesis (≤100 °C), the smectite-to-illite transformation and alkali-feldspar albitization (*c.* 80–150 °C), and the progressive recrystallization of sheet silicates (≥200 °C). Figure 8 shows the inferred pore fluid evolution for the Ultrahelvetic and South-Helvetic flysch units as a function of temperature and diagenetic-metamorphic processes. Notably, the trends for the flysch units are not identical, which most likely reflects differences in seawater signature and sedimentological composition. Independently from this variation, the bulk pore fluid evolution appears to be unaffected by the influx of external metamorphic fluids. A local mixture of diagenetic fluids with similar $^{87}Sr/^{86}Sr$ ratios, for example, during imbricate thrusting, can, however, not be excluded.

Our analysis shows that the Sr isotope systematics of vein carbonates sampled along a 30 km long transect and from a variety of outcrops, rock units and structures can provide consistent information that helps to understand the evolution of the thrust belt and the sequence of formation of distinct deformation structures, which was not sufficiently clear from field observations. In particular, our findings indicate that the emplacement of the Ultrahelvetic flysch onto the South-Helvetic flysch as well as the transport of the South-Helvetic thrust slice and related mélange formation occurred at diagenetic conditions of *c.* 100–150 °C. This suggests that the Ultrahelvetic and South-Helvetic flysch units were first underthrust and then accreted to the base of the wedge at some kilometres depth (Fig. 9a). Shearing during underthrusting is probably recorded by G_1 calcite shear veins that document a less-evolved fluid than the veins related to imbricate thrusting. After or during imbrication, slices of South-Helvetic flysch were displaced towards the foreland, probably by dragging the slices along the Penninic basal thrust that accommodated the underthrusting of the European continental margin until early Miocene time (e.g. Cardello *et al.* 2019). Out-of-sequence thrusting along the Glarus thrust and the related emplacement of the Helvetic nappes on top of the IFUs resulted in peak metamorphic conditions (Fig. 9b). At this time, the flysch units were already folded and the folds experienced a late-stage brittle overprint, as indicated by the tension

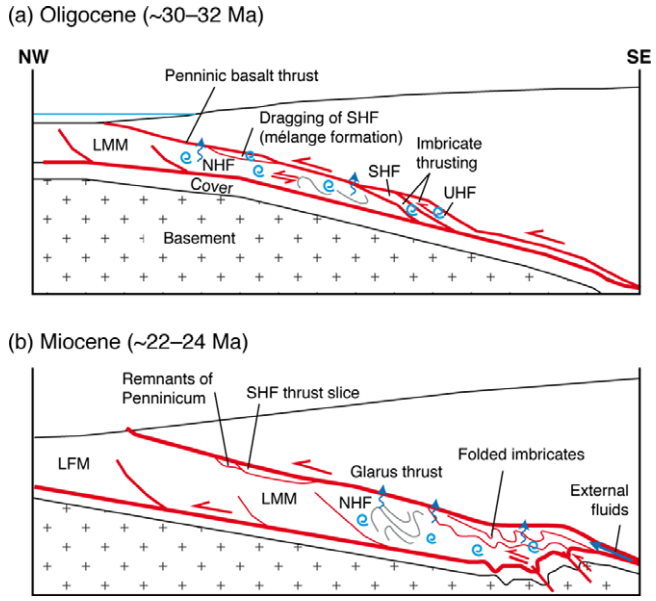

Fig. 9. Schematic cross-section illustrating the (a) diagenetic to (b) metamorphic evolution of the Infrahelvetic flysch units during the Alpine orogeny. LFM – Lower Freshwater Molasse; LMM – Lower Marine Molasse; NHF – North-Helvetic flysch; SHF – South-Helvetic flysch; UHF – Ultrahelvetic flysch. The blue arrows indicate fluid flow; the blue spirals indicate internal fluid evolution. Based on Burkhard *et al.* (1992), Dielforder *et al.* (2016) and Pfiffner (1986). Not to scale.

gashes. Otherwise, deformation was mainly related to the development of the pressure-solution cleavage and the formation of quartz-calcite veins (G_2 and G_3, veins, fissures). Finally, small thrusts developed in the North-Helvetic flysch during the late prograde to early retrograde evolution of the fold-and-thrust belt, which was potentially related to incipient deformation in the Aar massif.

Taken together, we have demonstrated that the Sr isotope systematics of vein carbonates can help to constrain the relative timing of deformation events within the tectonic and structural evolution of a fold-and-thrust belt. Our study benefited from good outcrop conditions and availability of data about the diagenetic to low-grade metamorphic evolution of the thrust belt. The presented approach may also be applicable to other thrust belts or to geological settings, with less structural control, such as active geothermal reservoirs or accretionary wedges. The Sr isotope systematics of vein carbonates recovered from drill cores from such settings may provide an easy means to disentangle deformation sequences and to identify fluid sources.

Supplementary material. To view supplementary material for this article, please visit https://doi.org/10.1017/S0016756821001357

Acknowledgements. Funding for this project was provided by the Swiss National Science Foundation (No. 144381). We thank H. Vollstaedt for discussion and support in the laboratory. The thoughtful and constructive reviews by Johannes Glodny and one anonymous reviewer are gratefully acknowledged. The authors declare that there is no conflict of interest.

References

Abart R, Badertscher N, Burkhard M and Povoden E (2002) Oxygen, carbon and strontium isotope systematics in two profiles across the Glarus thrust: implications for fluid flow. *Contributions to Mineralogy and Petrology* **143**, 192–208.

Akker IV, Berger A, Schrank CE, Jones MWM, Kewish CM, Klaver J and Herwegh M (2021a) The evolution of slate microfabrics during progressive accretion of foreland basin sediments. *Journal of Structural Geology* **150**, 104404. doi: 10.1016/j.jsg.2021.104404.

Akker IV, Berger A, Zwingmann H, Todd A, Schrank CE, Jones MWM, Kewish CM, Schmid TC and Herwegh M (2021b) Structural and chemical resetting processes in white mica and their effect on K–Ar data during low temperature metamorphism. *Tectonophysics* **800**, 228708. doi: 10.1016/j.tecto.2020.228708.

Awwiller DN (1993) Illite/smectite formation and potassium mass transfer during burial diagenesis of mudrocks: a study from the Texas gulf coast Paleocene–Eocene. *Journal of Sedimentary Petrology* **63**, 501–12.

Baccar MB, Fritz B and Made B (1993) Diagenetic albitization of K-feldspar and plagioclase in sandstone reservoirs: thermodynamic and kinetic modeling. *Journal of Sedimentary Research* **63**, 1100–9.

Badertscher NP, Abart R, Burkhard M and McCaig A (2002) Fluid flow pathways along the Glarus overthrust derived from stable and Sr-isotope patterns. *American Journal of Science* **302**, 517–47.

Beaudoin N, Lacombe O, Roberts NMW and Koehn D (2018) U–Pb dating of calcite veins reveals complex stress evolution and thrust sequence in the Bighorn Basin, Wyoming, USA. *Geology* **46**, 1015–18.

Bons PD, Elburg MA and Gomez-Rivas E (2012) A review of the formation of tectonic veins and their microstructures. *Journal of Structural Geology* **43**, 33–62.

Burkhard M (1990) Aspects of the large-scale Miocene deformation in the most external part of the Swiss Alps (Subalpine Molasse to Jura fold belt). *Eclogae Geologicae Helvetiae* **83**, 559–83.

Burkhard M, Kerrich R, Maas R and Fyfe WS (1992) Stable and Sr-isotope evidence for fluid advection during thrusting of the Glarus nappe (Swiss Alps). *Contributions to Mineralogy and Petrology* **112**, 293–311.

Cardello GL, Di Vincenzo G, Giorgetti G, Zwingmann H and Mancktelow N (2019) Initiation and development of the Pennine Basal Thrust (Swiss Alps): a structural and geochronological study of an exhumed megathrust. *Journal of Structural Geology* **129**, 338–56.

Cerchiari A, Remitti F, Mittempergher S, Festa A, Lugli F and Cipriani A (2020) Cyclical variations of fluid sources and stress state in a shallow megathrust-zone mélange. *Journal of the Geological Society, London* **177**, 647–59.

Clauer N and Chaudhuri S (1995) *Clays in Crustal Environments: Isotope Dating and Tracing*. New York: Springer, 369 pp.

Clauer N, Środoń J, Aubert A, Uysal IT and Toulkeridis T (2020) K–Ar and Rb–Sr dating of nanometer-sized smectite-rich mixed layers from bentonite beds of the Campos basin (Rio de Janeiro State, Brazil). *Clays and Clay Minerals* **68**, 446–64.

Dahlen FA (1990) Critical taper model of fold-and-thrust belts and accretionary wedges. *Annual Review of Earth and Planetary Sciences* **18**, 55–99.

Dielforder A, Berger A and Herwegh M (2016) The accretion of foreland basin sediments during early stages of continental collision and similarities to accretionary wedge tectonics. *Tectonics* **35**, 2216–38.

Dielforder A, Vollstaedt H, Vennemann T, Berger A and Herwegh M (2015) Linking megathrust earthquakes to brittle deformation in a fossil accretionary complex. *Nature Communications* **6**, 7504. doi: 10.1038/ncomms8504.

Dietrich D, McKenzie J and Song H (1983) Origin of calcite in syntectonic veins as determined from carbon isotope ratios. *Geology* **11**, 547–51.

Dodson MH (1973) Closure temperature in cooling geochronological and petrological systems. *Contributions to Mineralogy and Petrology* **40**, 259–74.

Ebert A, Herwegh M and Pfiffner A (2007) Cooling induced strain localization in carbonate mylonites within a large-scale shear zone (Glarus thrust, Switzerland). *Journal of Structural Geology* **29**, 1164–84.

El Meknassi S, Dera G, Cardone T, De Rafélis M, Brahmi C and Chavagnac V (2018) Sr isotope ratios of modern carbonate shells: good and bad news for chemostratigraphy. *Geology* **46**, 1003–6.

Elderfield H, Gieskes JM, Baker PA, Oldfield RK, Hawkesworth CJ and Miller R (1982) $^{87}Sr/^{86}Sr$ and $^{18}O/^{16}O$ ratios, interstitial water chemistry and diagenesis in deep-sea carbonate sediments of the Ontong Java Plateau. *Geochimica et Cosmochimica Acta* **46**, 2259–68.

Fagereng Å and Sibson RH (2010) Mélange rheology and seismic style. *Geology* **38**, 751–4.

Fagereng Å and Toy VG (2011) Geology of the earthquake source: an introduction. In *Geology of the Earthquake Source* (eds Å Fagereng and VG Toy), pp. 1–16. Geological Society of London, Special Publication no. 359.

Fantle MS and DePaolo DJ (2006) Sr isotopes and pore fluid chemistry in carbonate sediment of the Ontong Java Plateau: calcite recrystallization rates and evidence for a rapid rise in seawater Mg over the last 10 million years. *Geochimica et Cosmochimica Acta* **70**, 3883–904.

Festa A, Pini GA, Dilek Y and Codegone G (2010) Mélanges and mélange-forming processes: a historical overview and new concepts. *International Geology Review* **52**, 1040–105.

Fisher D and Byrne T (1987) Structural evolution of underthrusted sediments, Kodiak Islands, Alaska. *Tectonics* **6**, 775–93.

Ford M and Lickorish H (2004) Foreland basin evolution around the western Alpine Arc. In *Deep-water Sedimentation in the Alpine Basin of SE France: New Perspectives on the Gres d'Annot and Related Systems* (eds P Joseph and SA Lomas), pp. 39–63. Geological Society of London, Special Publication no. 221.

Frey M (1988) Discontinuous inversed metamorphic zonation, Glarus Alps, Switzerland: evidence from illite crystallinity data. *Schweizerische Mineralogische und Petrographische Mitteilungen* **86**, 171–84.

Frisch W (1979) Tectonic progradation and plate tectonic evolution of the Alps. *Tectonophysics* **60**, 121–39.

Gasser D and den Brok B (2008) Tectonic evolution of the Engi Slates, Glarus Alps, Switzerland. *Swiss Journal of Geosciences* **101**, 311–22.

Glodny J, Kühn A and Austrheim H (2008) Diffusion versus recrystallization processes in Rb–Sr geochronology: isotopic relics in eclogite facies rocks, Western Gneiss Region, Norway. *Geochimica et Cosmochimica Acta* **72**, 506–25.

Glotzbach C, Reinecker J, Danišík M, Rahn M, Frisch W and Spiegel C (2010) Thermal history of the central Gotthard and Aar massifs, European Alps: evidence for steady state long-term exhumation. *Journal of Geophysical Research: Solid Earth* **115**, F03017. doi: 10.1029/2009JF001304.

Handy MR, Schmid SM, Bousquet R, Kissling E and Bernoulli D (2010) Reconciling plate-tectonic reconstructions of Alpine Tethys with the geological-geophysical record of spreading and subduction in the Alps. *Earth-Science Reviews* **102**, 121–58.

Herwegh M, Berger A, Baumberger R, Wehrens P and Kissling E (2017) Large-scale crustal-block-extrusion during late Alpine collision. *Scientific Reports* **7**, 413. doi: 10.1038/s41598-017-00440-0.

Herwegh M, Berger A, Glotzbach C, Wangenheim C, Mock S, Wehrens P, Baumberger R, Egli D and Kissling E (2020) Late stages of continent-continent collision: timing, kinematic evolution, and exhumation of the Northern rim (Aar Massif) of the Alps. *Earth-Science Reviews* **200**, 102959. doi: 10.1016/j.earscirev.2019.102959.

Herwegh M, Hürzeler J-P, Pfiffner OA, Schmid SM, Abart R and Ebert A (2008) The Glarus thrust: excursion guide and report of a field trip of the Swiss Tectonic Studies Group (Swiss Geological Society, 14. – 16.09.2006). *Swiss Journal of Geosciences* **101**, 323–40.

Hilgers C and Sindern S (2005) Textural and isotopic evidence on the fluid source and transport mechanism of antitaxial fibrous microstructures from the Alps and the Appalachians. *Geofluids* **5**, 239–50.

Hubbert MK and Rubey WW (1959) Role of fluid pressure in mechanics of overthrust faulting. 1. Mechanics of fluid-filled porous solids and its application to overthrust faulting. *Bulletin of the Geological Society of America* **70**, 115–66.

Hunziker JC, Frey M, Clauer N, Dallmeyer RD, Friedrichsen H, Flehmig W, Hochstrasser K, Roggwiler P and Schwander H (1986) The evolution of illite to muscovite; mineralogical and isotopical data from the Glarus Alps, Switzerland. *Contributions to Mineralogy and Petrology* **92**, 157–80.

Jeanbourquin P (1994) Early deformation of Ultrahelvetic mélanges in the Helvetic nappes (western Swiss Alps). *Journal of Structural Geology* **16**, 1367–83.

Kempf O and Pfiffner OA (2004) Early Tertiary evolution of the North Alpine Foreland Basin of the Swiss Alps and adjoining areas. *Basin Research* **16**, 549–67.

Krabbenhöft A, Fietzke J, Eisenhauer A, Liebetrau V, Böhm F and Vollstaedt H (2009) Determination of radiogenic and stable strontium isotope ratios ($^{87}Sr/^{86}Sr$; $\delta^{88}/^{86}Sr$) by thermal ionization mass spectrometry applying an $^{87}Sr/^{86}Sr$ double spike. *Journal of Analytical Atomic Spectrometry* **24**, 1267–71.

Labaume P, Berty C and Laurent Ph (1991) Syn-diagenetic evolution of shear structures in superficial nappes: an example from the Northern Apennines (NW Italy). *Journal of Structural Geology* **18**, 385–98.

Lacroix B, Buatier M, Labaume P, Travé A, Dubois M, Charpentier D, Ventalon S and Convert-Gaubier D (2011) Microtectonic and geochemical characterization of thrusting in a foreland basin: example of the South-Pyrenean orogenic wedge (Spain). *Journal of Structural Geology* **33**, 1359–77.

Lahfid A, Beyssac O, Deville E, Negro F, Chopin C and Goffé B (2010) Evolution of the Raman spectrum of carbonaceous material in low-grade metasediments of the Glarus Alps (Switzerland). *Terra Nova* **22**, 354–60.

Lauer RM and Saffer DM (2015) The impact of splay faults on fluid flow, solute transport, and pore pressure distribution in subduction zones: a case study offshore the Nicoya Peninsula, Costa Rica. *Geochemistry, Geophysics, Geosystems* **16**, 1089–104.

Lihou JC (1995) A new look at the Blattengrat unit of eastern Switzerland: Early Tertiary foreland basin sediments from the South Helvetic realm. *Eclogae Geologicae Helvetiae* **88**, 91–114.

Lihou JC (1996a) Stratigraphy and sedimentology of the Sardona unit, Glarus Alps: Upper Cretaceous/middle Eocene deep-marine flysch sediments from the Ultrahelvetic realm. *Eclogae Geologicae Helvetiae* **89**, 721–52.

Lihou JC (1996b) Structure and deformational history of the Infrahelvetic flysch units, Glarus Alps, eastern Switzerland. *Eclogae Geologicae Helvetiae* **89**, 439–60.

Machel HG, Cavell PA and Patey KS (1996) Isotopic evidence for carbonate cementation and recrystallization, and for tectonic expulsion of fluids into the Western Canada Sedimentary Basin. *Geological Society of America Bulletin* **108**, 1108–19.

Mangenot X, Tarantola A, Mullis J, Girard JP, Le VH and Eiler JM (2021) Geochemistry of clumped isotopologues of CH_4 within fluid inclusions in Alpine tectonic quartz fissures. *Earth and Planetary Science Letters* **561**, 116792. doi: 10.1016/j.epsl.2021.116792.

McArthur JM, Howarth RJ and Bailey TR (2001) Strontium isotope stratigraphy: LOWESS Version 3: best fit to the marine Sr-isotope curve for 0–509 Ma and accompanying look-up table for deriving numerical age. *The Journal of Geology* **109**, 155–70.

McCaig AM, Wayne DM, Marshall JD, Banks D and Henderson I (1995) Isotopic and fluid inclusion studies of fluid movement along the Gavarnie thrust, central Pyrenees: reaction fronts in carbonate mylonites. *American Journal of Science* **295**, 309–43.

McLennan SM, Taylor SR, McCulloch MT and Maynard JB (1990) Geochemical and Nd–Sr isotopic composition of deep-sea turbidites: crustal evolution and plate tectonic associations. *Geochimica et Cosmochimica Acta* **54**, 2015–50.

Milliman JD (1974) *Marine Carbonates: Recent Sedimentary Carbonates. Part 1*. New York: Springer, 375 pp.

Milnes AG and Pfiffner OA (1977) Structural development of the Infrahelvetic complex, eastern Switzerland. *Eclogae Geologicae Helvetiae* **70**, 83–95.

Mittempergher S, Cerchiari A, Remitti F and Festa A (2017) From soft sediment deformation to fluid assisted faulting in the shallow part of a subduction megathrust analogue: the Sestola Vidicatico tectonic unit (Northern Apennines, Italy). *Geological Magazine* **155**, 438–50.

Mock S, von Hagke C, Schlunegger F, Dunkl I and Herwegh M (2020) Long-wavelength late-Miocene thrusting in the north Alpine foreland: implications for late orogenic processes. *Solid Earth* **11**, 1823–47.

Moore JC, Rowe C and Meneghini F (2007) How accretionary prisms elucidate seismogenesis in subduction zones. In *The Seismogenic Zone of Subduction Thrust Faults* (eds TH Dixon and JC Moore), pp. 288–315. New York: Columbia University Press.

Moore JC and Saffer DM (2001) Updip limit of the seismogenic zone beneath the accretionary prism southwest Japan: an effect of diagenetic to low-grade metamorphic processes and increasing effective stress. *Geology* **29**, 183–6.

Mullis J, Mählmann RF and Wolf M (2017) Fluid inclusion microthermometry to calibrate vitrinite reflectance (between 50 and 270°C), illite Kübler-Indes data and the diagenesis/anchizone boundary in the external part of the Central Alps. *Applied Clay Science* **143**, 307–19.

Nibourel L, Berger A, Egli D, Heuberger S and Herwegh M (2021) Structural and thermal evolution of the eastern Aar Massif: insights from structural field work and Raman thermometry. *Swiss Journal of Geosciences* **114**, 9. doi: 10.1186/s00015-020-00381-3.

Nibourel L, Berger A, Egli D, Luensdorf NK and Herwegh M (2018) Large vertical displacement of a crystalline massif recorded by Raman thermometry. *Geology* **46**, 879–82.

Nier AO (1938) The isotopic constitution of strontium, barium, bismuth, thallium and mercury. *Physical Reviews* **54**, 275–8.

Pfiffner OA (1986) Evolution of the north Alpine foreland basin in the central Alps. In *Foreland Basins* (eds PA Allen and P Homewood), pp. 219–28. Special Publications of the International Association of Sedimentologists no 8. Oxford: Blackwell Scientific.

Pfiffner OA (2011) Structural Map of the Helvetic Zone of the Swiss Alps, including Vorarlberg (Austria) and Haute Sovie (France), 1:100000. Geological Special Map 128. Explanatory Notes. Wabern: Federal Office of Topography Swisstopo.

Pytte AM and Reynolds RC (1989) The thermal transformation of smectite to illite. In *Thermal History of Sedimentary Basins* (eds ND Naeser and TH McCulloh), pp. 133–40. Berlin: Springer.

Rahn MK, Hurford AJ and Frey M (1997) Rotation and exhumation of a thrust plane: apatite fission-track data from the Glarus thrust, Switzerland. *Geology* **25**, 599–602.

Rahn M, Mullis J and Erdelbrock K (1995) Alpine metamorphism in the North Helvetic Flysch of the Glarus Alps, Switzerland. *Eclogae Geologicae Helvetiae* **88**, 157–78.

Remitti F, Bettelli G and Vannucchi P (2007) Internal structure and tectonic evolution of an underthrust tectonic mélange: the Sestola-Vidiciatico tectonic unit of the Northern Apennines, Italy. *Geodinamica Acta* **20**, 37–51.

Richter FM and Liang Y (1993) The rate and consequences of Sr diagenesis in deep-sea carbonates. *Earth and Planetary Science Letters* **117**, 553–65.

Sample JC (2010) Stable isotope constraints on vein formation and fluid evolution along a recent thrust fault in the Cascadia accretionary wedge. *Earth and Planetary Science Letters* **293**, 300–12.

Sample JC and Kopf A (1995) Isotope geochemistry of syntectonic carbonate cements and veins from the Oregon margin: implications for the hydrogeologic evolution of the accretionary wedge. In *Proceedings of the Ocean Drilling Program, Scientific Results, vol. 146* (eds B Carson, GK Westbrook, RJ Musgrave and E Suess), pp. 137–48. College Station, Texas.

Sample JC, Torres ME, Fisher A, Hong W-L, Destringeville C, Defliese WF and Tripati AE (2017) Geochemical constraints on the temperature and timing of carbonate formation and lithification in the Nankai Trough, NanTroSEIZE transect. *Geochimica et Cosmochimica Acta* **198**, 92–114.

Schmid SM (1975) The Glarus overthrust: field evidence and mechanical model. *Eclogae Geologicae Helvetiae* **68**, 247–80.

Schmid SM, Pfiffner OA, Froitzheim N, Schönborn G and Kissling E (1996) Geophysical-geological transect and tectonic evolution of the Swiss-Italian Alps. *Tectonics* **15**, 1036–64.

Sharp ZD and Kirschner DL (1995) Quartz-calcite oxygen isotope thermometry: a calibration based on natural isotope variations. *Geochimica et Cosmochimica Acta* **58**, 4491–501.

Sibson RH (1977) Fault rocks and fault mechanisms. *Journal of the Geological Society, London* **133**, 191–213.

Sibson RH (1998) Brittle failure mode plots for compressional and extensional tectonic regimes. *Journal of Structural Geology* **20**, 655–60.

Sibson RH (2013) Stress switching in subduction forearcs: implications for overpressure containment and strength cycling on megathrusts. *Tectonophysics* **600**, 142–52.

Sinclair HD (1997) Flysch to molasse transition in peripheral foreland basins: the role of the passive margin breakoff. *Geology* **25**, 1123–6.

Sinclair HD and Allen PA (1992) Vertical versus horizontal motions in the Alpine orogenic wedge: stratigraphic response in the foreland basin. *Basin Research* **4**, 215–32.

Takeshita T, Yamaguchi A and Shigematsu N (2014) Stress reversal recorded in calcite vein cuttings from the Nankai accretionary prism, southwest Japan. *Earth, Planets and Space* **66**, 144. doi: 10.1186/s40623-014-0144-4.

Tarantola A, Mullis J, Guillaume D, Dubessy J, de Capitani C and Abdelmoula M (2009) Oxidation of CH_4 to CO_2 and H_2O by chloritization of detrital biotite at 270 ± 5 °C in the external part of the Central Alps, Switzerland. *Lithos* **112**, 497–510.

Tarantola A, Mullis J, Vennemann T, Dubessy J and de Capitani C (2007) Oxidation of methane at the CH_4/H_2O–(CO_2) transition zone in the external

part of the Central Alps, Switzerland: evidence from stable isotope investigations. *Chemical Geology* **237**, 329–57.

Travé A, Labaume P, Calvet F and Soler A (1997) Sediment dewatering and pore fluid migration inferred from isotopic and elemental geochemical analyses (Eocene southern Pyrenees, Spain). *Tectonophysics* **282**, 375–98.

Ujiie K, Saishu H, Fagereng Å, Nishiyama N, Otsubo M, Masuyama H and Kagi H (2018) An explanation of episodic tremor and slow slip constrained by crack-seal veins and viscous shear in subduction mélange. *Geophysical Research Letters* **45**, 5371–9.

van de Kamp PC (2008) Smectite-illite-muscovite transformations, quartz dissolution, and silica release in shales. *Clays and Clay Minerals* **56**, 66–81.

Veizer J, Ala D, Azmy K, Bruckschen P, Buhl D, Bruhn F, Carden GAF, Diener A, Ebneth S, Godderis Y, Jasper T, Korte C, Pawellek F, Podlaha O and Strauss H (1999) $^{87}Sr/^{86}Sr$, $\delta^{13}C$ and $\delta^{18}O$ evolution of Phanerozoic seawater. *Chemical Geology* **161**, 59–88.

Villa IM (1998) Isotopic closure. *Terra Nova* **10**, 42–7.

Villa IM (2016) Diffusion in mineral geochronometers: present and absent. *Chemical Geology* **420**, 1–10.

Voigt J, Hathorne ED, Frank M, Vollstaedt H and Eisenhauer A (2015) Variability of carbonate diagenesis in equatorial Pacific sediments deduced from radiogenic and stable Sr isotopes. *Geochimica et Cosmochimica Acta* **148**, 360–77.

von Hagke C, Cederbom CE, Oncken O, Stöckli DF, Rahn MK and Schlunegger F (2012) Linking the northern Alps with their foreland: the latest exhumation history resolved by low-temperature thermochronology. *Tectonics* **31**, TC5010. doi: 10.1029/2011TC003078.

Vroliijk P, Myers G and Moore JC (1988) Warm fluid migration along tectonic melanges in the Kodiak accretionary complex, Alaska. *Journal of Geophysical Research* **93**, 10313–24.

Wang K (1994) Kinematic models of dewatering accretionary prisms. *Journal of Geophysical Research* **99**, 4429–38.

https://doi.org/10.1017/S0016756821001357 Published online by Cambridge University Press